Nanoscale

RSC Publishing

PAPER

View Article Online
View Journal | View Issue

Cite this: *Nanoscale*, 2013, **5**, 11499

Manganese-impregnated mesoporous silica nanoparticles for signal enhancement in MRI cell labelling studies†

Rémy Guillet-Nicolas,[abcd] Myriam Laprise-Pelletier,[bcd] Mahesh M. Nair,[ab] Pascale Chevallier,[d] Jean Lagueux,[d] Yves Gossuin,[e] Sophie Laurent,[f] Freddy Kleitz*[ab] and Marc-André Fortin*[bcd]

Mesoporous silica nanoparticles (MSNs) are used in drug delivery and cell tracking applications. As Mn^{2+} is already implemented as a "positive" cell contrast agent in preclinical imaging procedures (in the form of $MnCl_2$ for neurological studies), the introduction of Mn in the porous network of MSNs would allow labelling cells and tracking them using MRI. These particles are in general internalized in endosomes, an acidic environment with high saline concentration. In addition, the available MSN porosity could also serve as a carrier to deliver medical/therapeutic substances through the labelled cells. In the present study, manganese oxide was introduced in the porous network of MCM-48 silica nanoparticles (Mn–M48SNs). The particles exhibit a narrow size distribution (~140 nm diam.) and high porosity (~60% vol.), which was validated after insertion of Mn. The resulting Mn–M48SNs were characterized by TEM, N_2 physisorption, and XRD. Evidence was found with H_2-TPR, and XPS characterization, that Mn(II) is the main oxidation state of the paramagnetic species after suspension in water, most probably in the form of Mn–OOH. The colloidal stability as a function of time was confirmed by DLS in water, acetate buffer and cell culture medium. In NMR data, no significant evidence of Mn^{2+} leaching was found in Mn–M48SNs in acidic water (pH 6), up to 96 hours after suspension. High longitudinal relaxivity values of $r_1 = 8.4\ mM^{-1}\ s^{-1}$ were measured at 60 MHz and 37 °C, with the lowest relaxometric ratios ($r_2/r_1 = 2$) reported to date for a Mn–MSN system. Leukaemia cells (P388) were labelled with Mn–M48SNs and nanoparticle cell internalization was confirmed by TEM. Finally, MRI contrast enhancement provided by cell labelling with escalated incubation concentrations of Mn–M48SNs was quantified at 1 T. This study confirmed the possibility of efficiently confining Mn into M48SNs using incipient wetness, while maintaining an open porosity and relatively high pore volume. Because these Mn-labelled M48SNs express strong "positive" contrast media properties at low concentrations, they are potentially applicable for cell tracking and drug delivery methodologies.

Received 8th June 2013
Accepted 3rd October 2013

DOI: 10.1039/c3nr02969g

www.rsc.org/nanoscale

1. Introduction

In recent years, magnetic resonance imaging (MRI) has emerged as one of the most promising modalities enabling cell tracking *in vivo*.[1] Images of high anatomical resolution and excellent contrast in soft tissues are possible with MRI, without using ionizing radiation. As such, MRI is an optimal choice for preclinical and clinical studies where the precise detection and biodistribution of injected cells over time are mandatory.[1] For this, the cells must be labelled with contrast agents (CAs) prior to injection, in order to allow their visualization.

One of the most common CAs is iron-containing particles (SPIOs and USPIOS for example). They have been used for cell tracking in MRI since the beginning of the 1990s.[2–4] Because these superparamagnetic particles produce hypointense regions in MR images, *i.e.* strong signal attenuation due to T_2 shortening and T_2^* effects, they are designated as "negative" CAs.

[a]*Département de chimie, Université Laval, Québec, QC G1V 0A6, Canada. E-mail: freddy.kleitz@chm.ulaval.ca; Fax: +1 418-656-7916; Tel: +1 418-656-7812*

[b]*Centre de recherche sur les matériaux avancés (CERMA), Université Laval, Québec, QC G1V 0A6, Canada*

[c]*Département de génie des mines, de la métallurgie et des matériaux, Université Laval, Québec, QC G1V 0A6, Canada*

[d]*Axe Médecine Régénératrice, Centre de recherche du Centre hospitalier universitaire de Québec (AMSVR-CRCHUQ), 10 rue de l'Espinay, Québec, QC G1L 3L5, Canada. E-mail: marc-andre.fortin@gmn.ulaval.ca; Fax: +1 418-656-5343; Tel: +1 418-656-8682*

[e]*Service de physique expérimentale et biologique, Université de Mons, 20, Place du Parc, Mons, Belgium*

[f]*Service de chimie générale, organique et biomédicale, Université de Mons, Mons, B7000, Belgium*

† Electronic supplementary information (ESI) available: TEM images, particle size distributions, XRD, TPR, magnetometric profiles, T_1 and T_2 measurements at 60 MHz over time, NMRD profiles of materials, P388 cell proliferation assay after 4 h and T_1-w. MR images of P388 cells incubated with a solution of M48SNs. See DOI: 10.1039/c3nr02969g

Despite their indisputable advantages, T_2/T_2^* CAs suffer from limitations that prevent their use in many cell tracking applications.[5–8] Indeed, it is sometimes difficult to accurately distinguish iron oxide-labelled cells from other sources of hypointense regions such as blood clots, tissue–air interfaces or calcification areas.[8] Additionally, they usually induce magnetic susceptibility artefacts, which extend far beyond the volume of the labelled cells,[5–7] ultimately complicating cell tracking and quantification based on contrast differences. On the other hand, "positive" CAs (T_1-weighted), in spite of their lower intrinsic detection sensitivity limits, are less prone to image artefacts.[9–11] Such systems now represent a promising alternative to iron oxide particles for the MRI detection of thousands of cells injected, or accumulated, in a focal point *in vivo*.

A vast majority of positive MRI CAs are based on Gd^{3+}.[12,13] This paramagnetic rare-earth metal efficiently generates hyperintense regions in MR images by dramatically shortening the longitudinal relaxation time (T_1) of neighbouring protons. Most of the Gd-based contrast agents are based on small Gd chelates which are not efficiently internalised or retained by cells.[14–16] Therefore, alternatives to Gd chelates have been developed in the form of Gd-containing nanocrystals (Gd_2O_3, GdF_3, (Na/K)GdF_4, $GdPO_4$, *etc.*).[17–23] Cells labelled with Gd-based nanocrystals can be implanted and efficiently detected by MRI. Image artefacts were not reported with such nanoparticles used for "positive contrast" in T_1-weighted cell tracking procedures. In fact, contrast differences based on signal enhancement could be more quantitative than the susceptibility-induced negative contrast generated by SPIOs and USPIOs.

Mesoporous silica nanoparticles (MSNs) have been extensively used in nanomedicine and are emerging as promising drug delivery vectors.[24–27] Adequately labelled with paramagnetic ions, they can be exploited in theranostic applications.[24–29] They exhibit high porosity, high specific surface area, and tailored pore morphologies. They also express versatile inner and outer surface characteristics enabling different grafting procedures. MSNs are also very well tolerated by cells.[24,27,29,30] Mesoporous silica layers have been successfully used to coat magnetic nanoparticles, while preserving a certain interaction of hydrogen protons with the paramagnetic ions.[31–34] Gd ions were also grafted in MSNs, and the relaxometric properties of such constructs were characterized.[35–40] Gd–MSNs have thus been proposed for cell tracking applications using MRI.[41–43] However, the ion Gd^{3+} is associated with the occurrence of nephrogenic systemic fibrosis (NSF),[44] and concerns related to this disease have led to a resurgence of interest in Mn^{2+}-based contrast agents.

Mn^{2+} has been used since the inception of MRI.[45,46] The magnetic moment of Mn^{2+} (5 unpaired electrons on the 3d orbital) is lower than that of Gd^{3+} (7 unpaired electrons on the 4f orbital). However, Mn^{2+} is less toxic than the lanthanide, and the presence of Mn^{2+} in tissues is acceptable below certain toxicity thresholds, *i.e.* a serum concentration of 0.5–1.2 $\mu g\ L^{-1}$ is essential for normal development and body function.[47] In fact, the ion Mn^{2+} is currently used as a contrast agent for neurological applications,[48] and for cell labelling studies.[49] In this latter application, both the nature and the concentration of the Mn-based CAs internalized by the cells are of prime importance as they are susceptible to affect cellular proliferation and viability. Noticeably, MnO nanocrystals were shown to be safer than $MnCl_2$ salts at cellular concentrations required to reach T_1-weighted MRI detection thresholds.[49] Nevertheless, very few studies have so far been reported on the integration of Mn^{2+} ions in MSNs, for the purpose of enhancing the contrast of silica colloids for MRI. The first attempt to graft Mn^{2+} ions in silica mesopores was performed using an *in situ* chemical oxidation–reduction process.[50] After calcination and H_2 reduction, the Mn–MSNs were suspended in water. The longitudinal and transversal relaxivities at 3.0 T (r_1 = 2.28 and r_2 = 15.9 $mM^{-1}\ s^{-1}$, respectively), were much lower compared to Gd-labelled MSNs.[35–40] By using a similar synthesis approach for confining Mn species into the mesopores of hollow mesoporous silica nanoparticles (HMSNs), Shi and co-workers reported a rather low chemical stability for these systems.[51] The release of free Mn^{2+} ions was quickly observed under weak acidic conditions, as typically found in endosomes or in the microenvironment of tumours. Such leaching was found responsible for significantly enhancing the performance of Mn–HMSNs as positive MRI CAs. Relaxometric properties of the system in slightly acidic pH ($r_1 = 8.81\ mM^{-1}\ s^{-1}$ and $r_2 = 51.9\ mM^{-1}\ s^{-1}$) increased noticeably compared to those in a physiological pH ($r_1 = 0.79\ mM^{-1}\ s^{-1}$ and $r_2 = 27.7\ mM^{-1}\ s^{-1}$, $r_2/r_1 = 35$).

The performance of MRI CAs is also characterized by the r_2/r_1 ratio, which must be as close as possible to 1 for positive contrast (in T_1-w. imaging). Until now, in the best cases, r_2/r_1 close to ~6 was measured for Mn–MSNs.[50,51] Therefore, the relaxometric properties of Mn-grafted MSNs must still be improved substantially, to allow efficient tracking of MSNs by MRI in cellular labelling, drug delivery, and other theranostic applications. Also, more insights into the chemical and colloidal stability of paramagnetic oxides/silicates–MSNs are required before considering a safe use as MRI positive CAs. With the entry of MSNs in the pre-clinical development stage for biomedical applications, addressing safety issues associated with their use is urgently needed.[52] A few previous studies have described Mn-impregnated mesoporous silica materials.[50,51,53–57] However, the stability of Mn grafted in the porous network of MSNs, and suspended in water, has never been comprehensively characterized. Aqueous stability is a critical aspect of this technology. Moreover, advanced relaxometric study of Mn-labelled MSNs is still needed, to evaluate the true potential of such products for "positive" contrast in T_1-weighted MRI applications.

In order to address the above issues, we here report on the synthesis, characterization and stability assessment of highly porous Mn–MSNs with a 3-D mesostructure ($MnSi_xO_y$–MSNs). The resulting Mn–M48SN particles were characterized in terms of porosity, structure and composition by nitrogen physisorption at 77 K, transmission electron microscopy (TEM), powder X-ray diffraction (XRD), X-ray photoelectron spectroscopy (XPS) and temperature-programmed reduction (H_2-TPR). In addition, a comprehensive investigation of the colloidal stability of the system was performed in ultrapure water (pH 6) and acid buffers (pH 5), up to 96 hours. The relaxometric performance of the particle suspensions, as well as potential leaching of Mn^{2+} ions,

were measured and studied. Most importantly, NMRD profiles were obtained at varying magnetic field strengths and as a function of the soaking time in different buffers. P388 leukaemia cells were labelled with Mn–MSNs, their viability was assessed, and the MRI contrast enhancement obtained in T_1-w. MRI was evaluated. Finally, labelled cells were imaged by MRI. Contrast enhancement over time was used to demonstrate the potential of Mn–M48SNs for cell tracking in T_1-w. MRI.

2. Experimental section

2.1. Materials

n-Cetyltrimethylammonium bromide (CTAB, 99%), Pluronic F127 ($EO_{106}PO_{70}EO_{106}$, BioReagent) and tetraethylorthosilicate (TEOS, 98%) were purchased from Sigma-Aldrich, Canada. Manganese nitrate hydrate, $Mn(NO_3)_2{\cdot}xH_2O$ (99.9%, $x = 4$–6), was purchased from Alfa Aesar, Canada. All other chemicals and solvents were of analytical grade and were used without further purification unless otherwise specified.

2.2. Synthesis of MCM-48 nanoparticles

MCM-48 mesoporous silica nanoparticles (M48SNs) with a 3-D cubic network of pores were synthesized according to a published protocol.[58] In a typical synthesis, 1.0 g of CTAB and 4.0 g of Pluronic F127 were dissolved in 298 mL of H_2O/NH_3/EtOH (NH_4OH(aq.) (2.9 wt %)/EtOH = 2.5/1 (v/v)). A clear homogeneous solution was obtained and then 3.6 g of TEOS was added at once to the mixture, which was stirred at high speed for 1 min. The reaction mixture was further kept for 24 h under static conditions in a capped polypropylene bottle at room temperature. The resulting white, solid material was isolated by centrifugation at 15 300 *g* for 25 min, re-dispersed twice in 200 mL of deionized water, isolated again by centrifugation and dried overnight in air at 70 °C. Finally, M48SNs were calcined at 550 °C (heating ramp was 1 °C min^{-1}) for 5 hours under air atmosphere.

2.3. Modification of M48SNs with Mn

Manganese ions were inserted in the porous network of M48SNs using the incipient wetness technique. In brief, 2.0 g of M48SNs, previously degassed overnight at 150 °C, were impregnated with anhydrous EtOH containing 4 mmol (1148 mg) of manganese nitrate hydrate. The impregnation required 1280 μL of EtOH, corresponding to 80% of the pore volume (based on N_2 physisorption measurements of the pristine M48SNs). Then, the materials were dried overnight under air at 40 °C and calcined at 500 °C with a 1 °C min^{-1} ramp also under air atmosphere. Materials were further left for 5 hours at 500 °C. In a subsequent step, Mn–M48SNs were reduced at 500 °C using a 1 °C min^{-1} ramp under H_2 (5%)/N_2 (95%) atmosphere during 5 hours. Materials loaded with manganese are referred to as Mn–M48SNs in the following.

2.4. Transmission electron microscopy (TEM)

M48SNs and Mn–M48SNs were left in ultrapure water for 0, 24, 48 or 96 hours at room temperature, and then dried. Samples of dried nanoparticles were quickly dispersed in methanol under ultra-sound, and deposited dropwise on a carbon-coated copper grid for TEM analysis using a Jeol JEM-1230 operated at 80 keV. Samples of nanoparticles dispersed in a cell culture medium were also embedded in resin (see Section 2.14), and then sliced into 60 nm layers, prior to observation at 200 keV (Jeol JEM-2100F).

2.5. X-ray diffraction (XRD)

Low- and wide-angle powder XRD measurements of M48SNs and Mn–M48SNs were performed with a Siemens D5000 (reflection, θ–θ configuration; CuKα: $\lambda = 1.541$ Å; 40 kV; 30 mA; 1–55° 2θ, step size: 0.02 2θ; 0.02 s per step). The Jade (v 2.1) software coupled with JCPDS and ICDD (2001 version) databases was used to analyse the XRD data.

2.6. Porosity measurements

Nitrogen adsorption–desorption isotherms were measured at liquid nitrogen temperature (77.3 K) using a Micromeritics ASAP 2010 volumetric adsorption analyser (Norcross, GA, USA). Prior to analysis, samples were degassed at 200 °C under a turbo molecular vacuum for at least 12 h. The Brunauer–Emmett–Teller (BET) equation was used to calculate the apparent surface area from adsorption data obtained at P/P_0 between 0.05 and 0.2. Total pore volume was estimated using the Gurvitch rule from the amount of nitrogen adsorbed at $P/P_0 = 0.95$, assuming that adsorption on the external surface was negligible compared to adsorption in pores. Pore size distributions were determined by using non-local density functional theory (NLDFT) methods considering sorption of nitrogen at 77.3 K in cylindrical silica pores.[59,60] The implemented NLDFT models were supplied by the Quantachrome Autosorb 1.55 software (Quantachrome Instruments, Boynton Beach, FL, USA).

2.7. Physicochemical surface analysis

To assess the binding state of O, Si, C and Mn, X-ray photoelectron spectroscopy (XPS) was performed with a PHI 5600-ci spectrometer (Physical Electronics, Eden Prairie, MN, USA). The main XPS chamber was maintained at a base pressure of $<8 \times 10^{-9}$ Torr. A monochromatic aluminium X-ray source (Al Kα = 1486.6 eV) at 200 W was used to record survey spectra (1400–0 eV) with charge neutralization, and the high-resolution spectra were obtained using a standard magnesium X-ray source (1253.6 eV) at 150 W with no charge neutralization. The detection angle was set at 45° with respect to the normal of the surface and the analysed area was 0.016 cm^2. High-resolution analyses were performed on the O (1s), Si (2p) and Mn (2p) peaks and the binding energy scale of the spectra was aligned on the C (1s) peak at 285 eV. Curve fittings for the high-resolution peaks were determined using the PHI software.

2.8. Temperature-programmed reduction by hydrogen (H_2-TPR)

The Mn oxidation state was probed by H_2-TPR using an RXM-100 multi-catalyst testing and characterization system from Advanced Scientific Design Inc. In a typical experiment, 50 mg of Mn–M48SNs were placed in a quartz reactor and pre-treated at 500 °C

for 1 h with a ramp of 5 °C min^{-1} under a helium flow of 20 mL min^{-1}. The sample was then allowed to cool down to room temperature under the same gas flow. Finally, TPR was carried out under a 10 mL min^{-1} flow rate of 5% H_2 in Ar. The temperature was increased from 25 to 700 °C with a ramp of 5 °C min^{-1}. The consumption of hydrogen was monitored by TCD.

2.9. Colloidal suspensions of Mn–M48SNs

Aqueous colloidal suspensions of Mn–M48SNs were prepared by dispersing 200 mg of Mn–M48SNs in 10 mL of ultrapure water (vortex shaking for 2 min followed by 30 min treatment in an ultrasonic bath at room temperature (RT), repeated twice). The opaque suspension was then centrifuged at 500 *g* for 10 min. Only the supernatant was collected (8 mL) and used for further characterization. A fraction of the nanoparticles agglomerates in the calcination step (Section 2.3), and cannot be suspended in water. We estimated the weight fraction of suspended particles to be 20–30% of the initial 200 mg of Mn–M48SNs. However, from the collected supernatant, the particles formed a very stable colloidal suspension (Fig. S6†), without evidence of sedimentation.

The hydrodynamic diameters and the colloidal stability of the suspended Mn–M48SNs were assessed by Dynamic Light Scattering (DLS) using a Malvern DTS Nano zetasizer 173° (equilibration time set to 3 min; 3 measurements taken on each sample; only quality criteria data accepted as valid results). Mn–M48SNs were also suspended and characterized in an acetate buffer (20 mM, pH 5) following the same procedure described above. Finally, static DLS measurements (described above) were compared with "dynamic" DLS measurements. For this, suspensions prepared as previously described were kept for t = 3 h, 24 h, and 48 h, then centrifuged (400 *g*, 10 min), and re-suspended in fresh ultrapure water or in an acetate buffer (pH 5), prior to DLS measurements.

2.10. Relaxometric analyses

^{1}H relaxometry. Dilutions of Mn–M48SN aqueous suspensions were prepared with ultrapure water (100, 50 (1 : 2), 25 (1 : 4), and 10% (1 : 10) (v/v)) and distributed in 10.0 mm NMR tubes. Longitudinal and transversal relaxation times (T_1 and T_2) were measured with a dedicated TD-NMR relaxometer (Bruker Minispec 60 mq, 60 MHz (1.41 T), 37 °C). To calculate the relaxivities, the amount of Mn in the aqueous suspensions was precisely measured by graphite furnace atomic absorption spectroscopy (GF-AAS; Perkin-Elmer Analyst 800). Prior to elemental analysis, dried samples of each suspension were digested overnight at 80 °C in HNO_3 (trace metal, Fisher Scientific A509–500). Solutions were then centrifuged, and the supernatant was diluted several times with Nanopure water. Relaxation rates ($1/T_1$ and $1/T_2$) were plotted against Mn concentration values and relaxivities (r_1 and r_2) were obtained by applying a linear regression of this plot. T_1 and T_2 of 100% (v/v) Mn–M48SNs suspended in acid buffers were also measured to evaluate the extent of leaching of Mn ions at pH = 5. For this, the suspensions were treated as described in Section 2.9 ("dynamic" measurements), prior to T_1 and T_2 measurements.

NMRD profiles. Longitudinal relaxivities (r_1) were measured on 100% (v/v) Mn–M48SN suspensions from 0.015 to 40 MHz with a Stelar fast field cycling relaxometer (Mede, Italy) set at 37 °C.

2.11. Cell labelling studies

For cell labelling studies, the suspensions of Mn–M48SNs were prepared by dispersing 75 mg of Mn–M48SNs in 3.75 mL of ultrapure water (vortex shaking for 2 min followed by 30 min treatment in an ultrasonic bath at RT, repeated twice). The suspension was then centrifuged at 1000 *g* for 10 min. The supernatant was collected (3 mL) and centrifuged at 4300 *g* for 10 min. The supernatant was discarded, and the particles were suspended in 3 mL of ultrapure water.

P388 leukaemia mouse cancer cells were maintained in a Roswell Park Memorial Institute medium (RPMI), in T-75 flasks, until they reached ~80% confluence. Before incubation with the nanoparticles, the cell concentration was adjusted to 2×10^6 cells per mL in complete Dulbecco's modified Eagle medium (DMEM) supplemented with D-glucose (4.5 g L^{-1}), L-glutamine, sodium pyruvate (110 mg L^{-1}), 10% inactive fetal bovine solution (FBS), and 1% streptomycin–penicillin (all products from GIBCO were used). For MRI studies, cells were maintained in Falcon tubes at 2×10^6 cells per tube. For the cell proliferation assays and experiments requiring prolonged incubation times (up to 24 h), concentrations of 6×10^5 cells per tube were used. Solutions were prepared by diluting 100% (v/v) Mn–M48SN stock colloidal suspensions with complete DMEM (1 : 14.3, 1 : 20, and 1 : 50 (v/v)). The cells were incubated at 37 °C in humidified 95% air/5% CO_2 with these solutions (2 mL per tube). For MRI studies and proliferation assays, cells were incubated for 4 hours with Mn–M48SNs. To avoid sedimentation of the cells, tubes were gently stirred every 20 minutes. To assess the viability of cells submitted to prolonged incubation with Mn–M48SNs, incubation times of 12 h and 24 h were used. Each cell culture condition was performed at least in quadruplicate. Incubation with complete DMEM was used as a control. After incubation, the cells were stained with Trypan blue and counted (number and viability) with an automated cell counter (Cellometer Auto T4, Nexcelom Bioscience, Lawrence, MA) within the first 20 minutes after harvest. The cells were centrifuged (400 *g*, 5 min), and suspended in 2 mL of complete DMEM. This procedure was repeated three times. Labelled cell suspensions were also sampled for TEM cell analysis. The remaining cells were suspended in 2% (w/v) gelatine (150 μL, bovine skin type B gelatine/serum-free DMEM) and distributed into 96-well plates prior to MR imaging.

2.12. Magnetic resonance imaging (MRI)

Plates containing contrast media and labelled cells suspended in gelatine were imaged with a 1.0 T preclinical MRI scanner (ASPECT Imaging, Netanya, Israel), using a custom-built microplate coil. A T_1-weighted 2D-spin echo sequence was used, with the following parameters: TE/TR = 11.2/400 ms; fα = 90°; FOV = 70 mm; 1.0 mm slices, 200 × 200; 3 excitations; 4 min acquisition time.

2.13. Contrast quantification

The contrast in MR images was quantified using the following equation:

$$\text{Contrast} = \frac{2(S_2 - S_1)}{S_2 + S_1}$$

where S_1 is the signal from a region of interest (ROI) drawn over the cell culture well containing non-labelled cells embedded in gelatine, and S_2 is the signal from the ROI of cells labelled with Mn–M48SNs, embedded in gelatine and imaged as described in Section 2.12.

2.14. TEM cell study

To visualize cell internalization of Mn–M48SN particles, 100 μL of the cell suspension was fixed for 24 h at 4 °C with 2.5% glutaraldehyde after treatment with a 0.001 M sodium cacodylate buffer (pH 7.3). The samples were dehydrated in a graded series of ethanol solutions, and embedded in Poly/Bed 812 epoxy resin (Polysciences Inc., Warrington, PA). Thin sections were processed and visualised using a JEOL JEM-2100F TEM system operated at 200 keV.

3. Results and discussion

3.1. Synthesis and porosity characterization of Mn–M48SNs

M48SN nanoparticles were synthesized according to a previously reported protocol.[58] The mesoporous particles were then impregnated with manganese nitrate dispersed in ethanol, followed by calcination and reduction at 500 °C allowing the synthesis of a Mn-containing phase inside the interwoven mesoporous channels of the M48SNs (Fig. 1). The resulting particles were deposited on TEM grids and imaged at 80 keV (ESI, Fig. S1a and Fig. S2†). TEM images of dried Mn–M48SNs revealed non-aggregated, well-defined and uniform spherical particles, with an average particle size of ~140 nm (Fig. S1d and Fig. S2, ESI†). Furthermore, samples of Mn–M48SN particles embedded in polymer resin, sliced at 60 nm and imaged (Fig. 1c), showed indications that electron beam-attenuating elements (*i.e.*, Mn) are located inside the silica particles and not only at their surface. The particles have also been visualised following different water soaking periods (Fig. 1a and Fig. S1b and c, ESI†). Both as-synthesized and water-dispersed Mn–M48SN particles revealed individualised nanoparticles of similar diameters and morphology. The outer surface of Mn-M48SNs was apparently not significantly affected by the impregnation step nor by the repeated thermal treatments. Moreover, no bulk manganese oxide particles were observed outside of the pores indicating the successful sequestration of Mn species inside the M48SNs. Low-angle X-ray diffraction (XRD) patterns of the Mn–M48SNs were characteristic of materials with mesoscopic order. The diffraction pattern of the M48SNs is commensurate with the body-centered cubic *Ia3d* symmetry (Fig. S3, ESI†). A noticeable loss in intensity and a slight shift of the main peak to higher 2θ values were noted in the low-angle X-ray diffraction patterns for the Mn-loaded materials compared to the pristine host. After thermal reduction, no evidence was found of wide-angle XRD peaks corresponding to crystalline MnO or Mn silicates. This might be due to the amorphous nature of the Mn species or very fine crystallite sizes, which could be too small to be discriminated by this technique.

After thermal reduction, Mn–M48SNs showed a typical type IV isotherm with a steep capillary condensation step, characteristic of an excellent quality mesoporous material with uniform mesopore size (Fig. 2a). Although the treatment with manganese did not cause obstruction of the pores, a marked decrease in all porosity features was observed for Mn–M48SNs compared to the pristine M48SNs (Table 1, Fig. 2). Indeed, the BET apparent specific surface area decreased from 1841 to 1365 $m^2\ g^{-1}$, the total pore volume decreased from 0.84 to 0.67 $cm^3\ g^{-1}$ and a slight decrease of the pore size was also observed, *i.e.* from 3.0 nm for M48SNs to 2.9 nm for Mn–M48SNs (Fig. 2b and Table 1), possibly caused by very thin layers of Mn species inside the pores. Similar observations were previously made in the case of Gd–M48SN analogues.[37]

The size of Mn–M48SN particles was not significantly affected after soaking in water for prolonged times (up to 96 h). In particular, the particle size distributions extracted from the TEM results (Fig. S1d, ESI†) after 24 h and 96 h of soaking were almost identical. However, the low-angle XRD patterns obtained for the Mn–M48SN particles soaked for 96 hours and dried did not show the peaks characteristic of the *Ia3d* symmetry. Also, a significant and progressive decrease in the signal-to-noise ratio was noted, indicating deterioration of the pore structure in

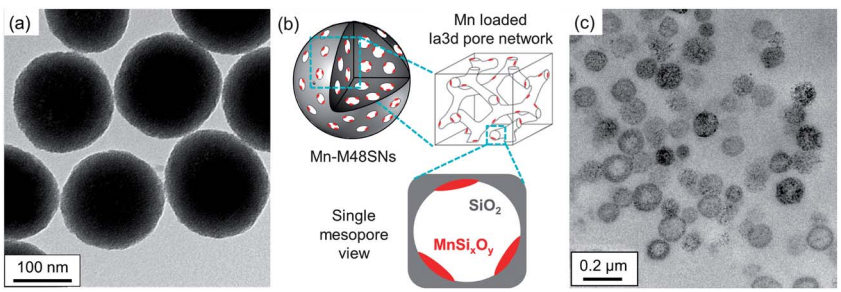

Fig. 1 (a) TEM images (80 keV) of Mn–M48SNs after thermal reduction treatment, and suspension in water for 3 h; (b) schematic representation of Mn–M48SNs; the 3-D mesopore network shows accessible porosity after impregnation with Mn and thermal treatments; and (c) TEM image of Mn–M48SNs embedded in a polymer resin, sliced at 60 nm and imaged at 200 keV.

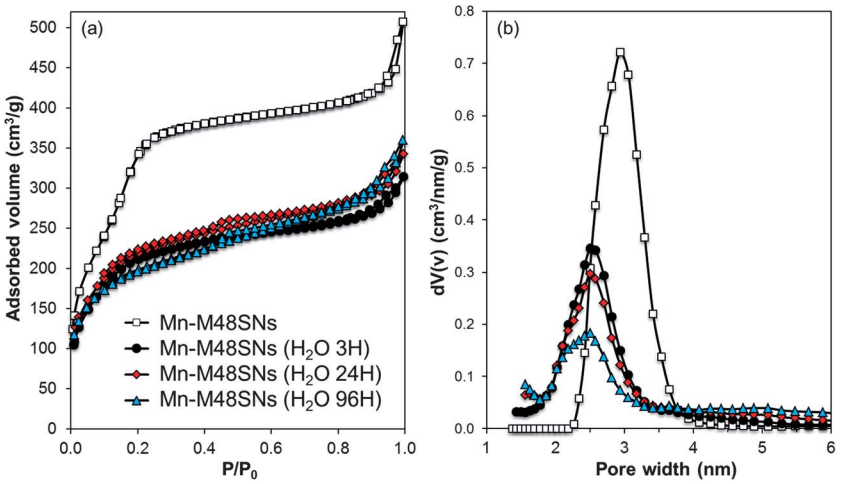

Fig. 2 (a) N_2 at 77 K adsorption/desorption isotherms and (b) corresponding NLDFT pore size distributions (from the adsorption branch) obtained for Mn–M48SNs after thermal reduction treatment and suspension in H_2O for various times.

Table 1 Textural properties of M48SNs and Mn–M48SNs suspended in Nanopure water for various times

Sample	BET specific surface area ($m^2\ g^{-1}$)	Pore volume ($cm^3\ g^{-1}$)	NLDFT ads. pore size (nm)
M48SNs	1841	0.84	3.0
Mn–M48SNs	1365	0.67	2.9
Mn–M48SNs (H_2O 3H)	805	0.44	2.6
Mn–M48SNs (H_2O 24H)	814	0.47	2.6
Mn–M48SNs (H_2O 96H)	723	0.48	2.5

aqueous media, which is in line with previous studies.[27,61,62] Based on the textural properties of the particles (Table 1) and the N_2 adsorption/desorption measurements (Fig. 2), it is clear that soaking in water has an immediate impact on the pore volume and the specific surface area. The pore volume of the particles decreased from 0.67 $cm^3\ g^{-1}$ to ~0.45 $cm^3\ g^{-1}$ after suspension in water. Between 3 h and 96 h however, no significant change in pore volume was noted. The only two indications of a structural change after prolonged soaking in water was noted by low-angle XRD (Fig. S3, ESI†), as well as TEM in Fig. S1c† (after 96 h), in which the particles have a more "sponge-like" appearance. The possible degradation of mesoporous silica nanoparticles in aqueous media has previously been documented.[27,61,62] Overall, in the present case, TEM and porosity measurements tend to confirm the adequate hydrolytic stability of the Mn–M48SN particles in aqueous suspensions.

3.2. Surface characterization and state of Mn in Mn–M48SNs

XPS. The elemental compositions of Mn–M48SNs were analysed by XPS (Table 2 and Fig. 3). The composition of Mn–M48SNs in water remained unchanged up to 24 h. After 96 h however, a slight decrease in Si was noted, as well as an increase in Mn. This observation, coupled with the evidence of MSN surface degradation shown by TEM visualisation, suggests that Mn is not located at the outer surface of as-synthesized Mn–M48SNs, but rather distributed inside the mesopore network. The increase of Mn after 96 h could also indicate the re-deposition of Mn–OOH species on the outer surface of particles, upon prolonged incubation in aqueous media. In fact, Mn (II, III, IV) oxides occur in numerous phases of variable structures that are enabled by the ability of their building unit, $Mn(O,OH)_6$ octahedra, to form infinite layers and three-dimensional structures. Several of these structures contain freely accessible interlayer spaces of various sizes, which could promote interactions with H_2O molecules.[63] As for any MSN system in aqueous media, a large content of Si–OH groups is also expected. Hydroxylation of MSN surfaces could explain the difference in O/Si ratios from a theoretical ratio of 2, to the slightly higher values observed with the materials investigated in the present study.

To further investigate the chemical environment of each species, high-resolution spectroscopy on O (1s), Si (2p) and Mn (2p), was performed. First, both O (1s) and Si (2p) were deconvoluted in 2 bands: one due to silica structure (533.3 eV and 104.4 eV respectively) and the other one from Mn–O–Si (530.9 eV and 102.0 eV).[64–66] This observation is consistent with previous results from our group, reported for a Si–O–Gd system,[37] and points to the presence of thin manganese silicate domains inside the pores (as schematically represented in Fig. 1b). However, it should be noted that the silicon peak characteristic of mesoporous silica was slightly shifted to higher energies compared to literature data (from ~103.8 to 104.4 eV in this study). We attribute this observation to the treatment performed in an aqueous environment, which could lead to a certain charge effect.

The Mn (2p3/2) feature centered at 641.2 eV matched with the typical binding energy of the metal-silicate (Mn–O–Si).[67] This peak was slightly shifted to higher energy, 641.4 eV, upon aging in water. Liu *et al.* have associated the Mn (2p3/2)

Table 2 Elemental contents of the particles (XPS)

Sample	% C	% O [O1 – 533.3 eV] (O2 – 530.8 eV)	% Si [Si1 – 104.4 eV] (Si2 – 102.0 eV)	O/Si [O1/Si1] (O2/Si2)	% Mn
Mn–M48SNs (H_2O 3H)	11.3	62.3 [43] (19.3)	24.7 [16.2] (8.5)	2.52 [2.65] (2.27)	1.6
Mn–M48SNs (H_2O 24H)	11.8	62.0 [46.9] (15.1)	24.8 [18.5] (6.3)	2.50 [3.10] (2.40)	1.4
Mn–M48SNs (H_2O 96H)	12.3	61.5 [48.5] (13.0)	23.6 [19.1] (4.5)	2.61 [2.54] (2.89)	2.6

centered at 641.6 eV with Mn–OOH species.[68] Therefore, it could be hypothesized that the initial Mn–O–Si at 641.2 eV was gradually transformed in Mn–OOH leading to a chemical shift towards high energy. Mn (2p3/2) peaks higher than 642 eV would have indicated the presence of higher oxidation states (*e.g.* Mn(III), Mn(IV)). The presence of a satellite peak at ~646–647 eV in the background also reflects the occurrence of Mn(II).[69–71] Finally, the separation of peak energies (ΔE_b) of the Mn (3s) components (data not shown) were found to be 6.1–6.2 eV before and after soaking in water, which also indicates Mn(II).[72] The presence of Mn(III) or Mn(IV) would imply $\Delta E_b < 5.0$. The Mn–OOH formation could also be corroborated by the increase of the ratio of the O band at 530.8 eV (Mn–O–Si, Mn–OOH) on that of Si at 102.0 eV (Si–O–Mn, Si–OH) from 2.27 to 2.89 after 96 hours (Table 2). Besides, the ratio of oxygen and silicon bands associated with the silica structure decreased from 2.65 to 2.54 , reflecting the modification of the M48SN structure during aqueous treatment.

TPR. Temperature-programmed reduction (H_2-TPR) profiles of Mn–M48SNs before and after soaking in ultrapure water, up to 96 h, are shown in Fig. S4 (ESI).† These profiles were also used to probe the oxidation states of Mn. For Mn–M48SNs, subjected to H_2-TPR immediately after the thermal reduction (Fig. S4a, ESI†), no noticeable peaks were obtained, indicating that this material only contains Mn species in the +2 oxidation state. Such a result is of importance to achieve a significant MR-contrast effect, as the paramagnetic moment of the Mn^{2+} ion allows for efficient interactions with hydrogen spins in biological tissues and aqueous media, resulting ultimately in dramatic reduction of longitudinal and transversal relaxation times. For the Mn–M48SNs suspended in water for 3 h and 24 h (Fig. S4b and c, ESI†), a broad hydrogen consumption peak centered slightly above 500 °C was observed along with a small shoulder appearing approximately at 360 °C. Interestingly, after 96 h in water, instead of a shoulder, a clearly distinguishable peak centered at about 320 °C was recorded. In all materials that were in contact with ultrapure water, the high temperature peak above 500 °C suggests the potential presence of Mn species in a higher oxidation state, which may result from the alteration/degradation of the Mn–M48SN framework during prolonged soaking in water. However, it should be noted that both XPS results and relaxometric studies tend to indicate that Mn species in higher oxidation states correspond only to a rather small fraction of the total Mn content in Mn–M48SNs. It is of particular importance that the shoulder observed at 360 °C for the Mn–M48SNs suspended in water for 3 h and 24 h indicates the presence of hydroxides or hydrated Mn species which is further confirmed by the apparition of a separate peak for the Mn–M48SNs suspended in water for 96 h. The first reduction process occurred at the lowest temperature for materials suspended in water for 96 h, indicating that prolonged exposure to aqueous media ultimately modified the local chemical environment of the metallic species. Even though a similar effect is observed for the second reduction step, the variation in

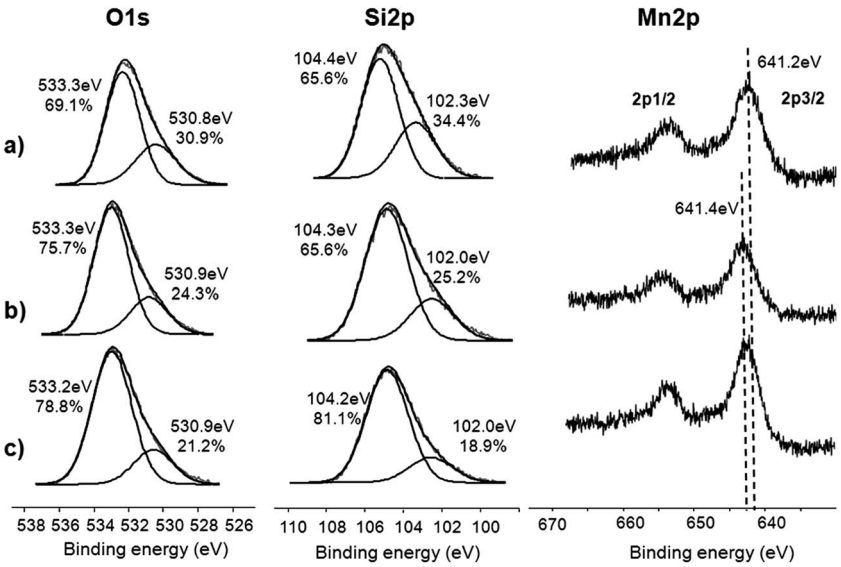

Fig. 3 O, Mn and Si high-resolution XPS spectra of (a) Mn–M48SNs after thermal reduction treatment and suspension in H_2O for (b) 3 h, (c) 24 h and (d) 96 h.

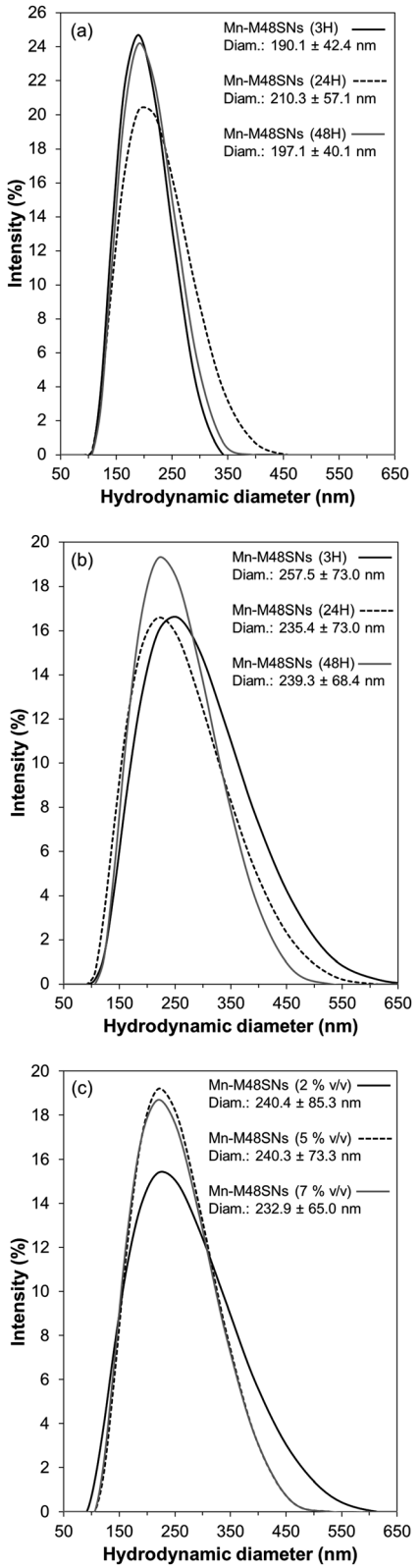

Fig. 4 Hydrodynamic diameter distributions of Mn–M48SNs after suspension in (a) H_2O or (b) acetate buffer (20 mM, pH = 5) for 3, 24 and 48 hours; (c) hydrodynamic diameter distributions of Mn–M48SNs after suspension in complete DMEM for two hours at various concentrations.

temperature is negligible considering the fact that the peaks are much broader. Such results are also consistent with the proposed gradual formation of Mn–OOH surface layers.

Magnetometry. The paramagnetic nature of Mn–M48SN powders was confirmed by magnetometric measurements conducted at 10, 100, 200 and 298 K. As shown in Fig. S5 (ESI)† the magnetic moment of the sample is proportional to the magnetic field at high temperatures. The typical curvature of the Langevin field dependence of the magnetization is only noticed at 10 K. The slope at low field of these curves is proportional to the zero field susceptibility, which obeys the Curie–Weiss law for paramagnetic systems. When plotted against temperature (inset of Fig. S5, ESI†), the slopes obtained for the Mn–M48SN powder are perfectly fitted by a $1/(T + T_0)$ function, which confirms the paramagnetic nature of the sample.

3.3. Colloidal stability of Mn–M48SNs

The particles were suspended in water by sonication and their colloidal stability, assessed by DLS for up to 48 h in water, acetate buffer and cell culture medium (DMEM). Although certain sedimentation was noted, the hydrodynamic diameter of the particles remained stable over time (Fig. 4a–c). A 24 h colloidal stability assay was performed in complete DMEM. Results from this study are shown in Fig. S6 (ESI)†. The mean particle size remained remarkably stable during this period (from 208 to 195 nm diam. in number-weighted data, for samples at $t = 0$ and $t = 24$ h, respectively). There was no evidence of sedimentation in DLS cells, and no fluctuation was noted in the attenuator aperture, which would have directly indicated the decrease of colloid concentration. Higher hydrodynamic diameters were measured in Mn–M48SNs in acetate and DMEM, which reflects the strong ionic corona (in acetate and DMEM) and protein adsorption (in DMEM).

3.4. Relaxivity and Mn chemical stability measurements

The performance of MRI CAs is always quantified on the basis of their longitudinal and transversal relaxivities ($1/T_1$ and $1/T_2$, normalised to the concentration of Mn). In this study, r_1 and r_2 relaxivities were first measured at 60 MHz (1.41 T), and showed values of 8.4 and 16.8 mM^{-1} s^{-1}, respectively (Fig. 5). These results appear much higher than relaxivity values typically measured for $MnCl_2$ (Mn^{2+} ions), in the order of 6.1 mM^{-1} s^{-1} for r_1 and $r_2/r_1 \sim 10$.[49,73] The relaxometric ratios ($r_2/r_1 = 2$) were remarkably small, and allowed much stronger "positive" contrast enhancement in MRI, than the vast majority of all Mn-containing CAs.[73] These relaxometric properties indicate that Mn in M48SNs is accessible to water molecules. Because the r_2/r_1 ratio of Mn-M48SN suspensions is so low, manganese is not in the form of free Mn^{2+} ions and this also corroborates the presence of MnO, Mn–O–Si and/or Mn–OOH structures in the mesopores. By comparison, for Mn–MCM-41 mesoporous silica nanoparticles impregnated with $KMnO_4$ and reduced in hydrogen, Shi *et al.* reported relaxivity values of $r_1 = 2.28$ and $r_2 = 15.9$ mM^{-1} s^{-1} ($r_2/r_1 = 6.97$) at 3.0 T.[50] Therefore, our study evidences that the procedure used to introduce and reduce manganese in the mesopore network has a very strong

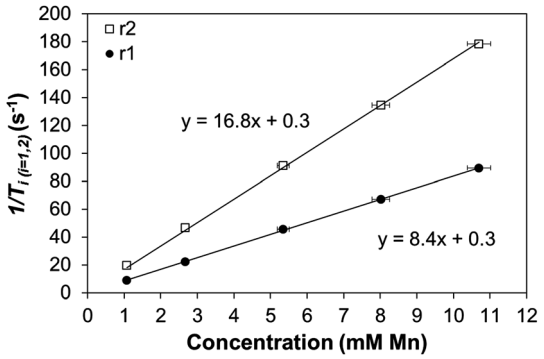

Fig. 5 Longitudinal (r_1, solid symbols) and transversal (r_2, open symbols) relaxivities of Mn–M48SNs in H_2O at 60 MHz and 37 °C.

incidence on the induction of high relaxivities (with low r_2/r_1 ratios), which are adequate for "positive" contrast enhancement in T_1-w. MRI.

In order to demonstrate the applicability of new CAs for cell tracking, it is necessary to quantify the chemical stability of the paramagnetic species submitted to an aqueous environment showing characteristics similar to those encountered in the cell vesicles. Lysosomes, endosomes, and phagosomes present an environment with pH as low as 4.5–5.[74–77] Depending on their resistance to acidic environments and to the reactive nature of their chemical form, silica and metal oxide nanoparticles taken up by cells and sequestered in these vesicles, are susceptible to dissolution.

Until now, stability tests of nanoparticulate MRI CAs have most often been conducted in an acetate buffer (*e.g.* pH 5, 20 mM).[78] However, such conditions are not representative of the endosome's content. In fact, the acidity of transition metal oxides is dependent on both the type and the oxidation state of the metal. Also, weak acids, such as acetic acid, act as proton donors and complexing agents that might accelerate the dissolution of certain oxides. Therefore, in the absence of a model solution that could reproduce the exact vesicular contents in a variety of cells, we decided to test Mn–M48SN particles in water, as well as in both acetate and borate buffers (pH 5, 20 mM). This approach revealed clear differences in the chemical stabilities of Mn–MSNs, depending on the selected buffer. The particles suspended in water, borate and acetate buffers were collected at different time points by centrifugation, and re-suspended in fresh ultrapure water, followed by T_1 and T_2 measurements at 60 MHz over time. The longitudinal and transversal relaxation times were used as a confirmation of Mn(II) retention. As expected, no significant evolution was found in T_1 and T_2 for particles suspended in water (Fig. S7a, ESI†), confirming the stability of Mn in the nanoparticle structure even after 96 hours of incubation.

In the acetate buffer however, Mn^{2+} ions rapidly leached and, as a result, much longer T_1 and T_2 were rapidly observed in the colloidal suspensions made with refreshed ultrapure water (Fig. S7b, ESI†). As previously mentioned in the TEM and porosity analysis section, the silica particles were not severely degraded after 96 h of soaking in water (Fig. S1c and d† and Table 1). However, a re-arrangement of the porous network was clearly noted, as well as the formation of Mn–OOH layers at the surface of pores (XPS and TPR results). Results of Fig. S7b† demonstrate that acetate does certainly interfere with the re-arrangement of Mn into Mn–OOH layers in the first minutes following dispersion in the buffer. Although acetate is frequently used to challenge the chemical and colloidal stability of colloidal nanoparticle systems, it is an aggressive buffer that unfortunately does not represent the exact same conditions as in the cell vesicles. Other buffers more closely mimicking the endosomal conditions should be selected for such studies.

To confirm the impact of an incubation buffer on the leaching of Mn^{2+} ions, nuclear magnetic resonance dispersion (NMRD) profiles ($1/T_1$) were recorded with a fast field relaxometer at variable magnetic field strength (Fig. 6 and S8, ESI†), with particles incubated in water, acetate, and borate buffers. NMRD profiles in water and in borate buffers showed a progressive decrease in the range 0.1–3 MHz, which is consistent with the mechanisms of proton relaxation by dipolar interactions between the coordinated water protons and the paramagnetic ions. This inflection is widely observed in paramagnetic complexes, such as EDTA or DTPA, as well as in suspensions of ultra-small MnO nanoparticles.[49,79] It is to be noted that the progressive decrease in $1/T_1$ relaxation rates observed in these measurements, mainly reflects the fact that particles had the tendency to sediment and adhere to the walls of NMRD tubes over time. Sonication was used between each NMRD measurement to suspend as much particles as possible and DLS analysis was performed each time to demonstrate that particles did not form aggregates upon sedimentation.

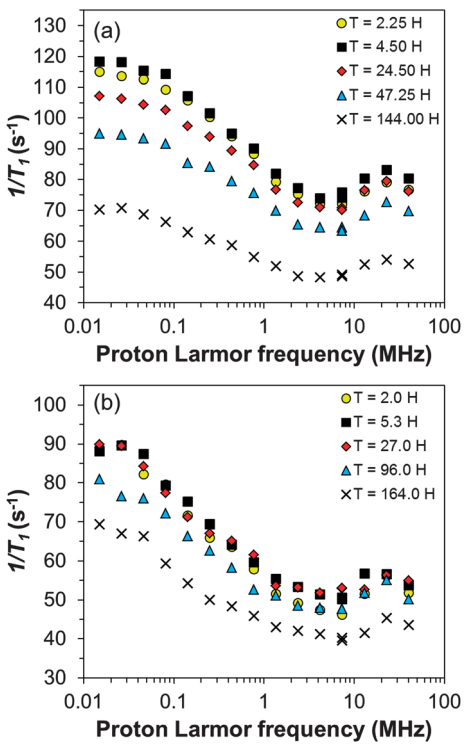

Fig. 6 NMRD profiles of Mn–M48SNs in (a) H_2O and (b) in a borate buffer (20 mM, pH = 5), both performed at 37 °C.

Table 3 Cell viability of P388 cells incubated for 4 h with Mn–M48SNs (2, 5, 7% (v/v))

% Mn–M48SNs (v/v)	Incubation time (h)	Mean number of cells $\times 10^6$	Standard dev. $\times 10^6$	Mean viability[a] (%)	Relative mean viability[b] (%)
0	4	1.70 ($n = 5$)	0.32	98.2	100
2	4	1.97 ($n = 5$)	0.42	97.3	99.1
5	4	1.54 ($n = 5$)	0.15	95.3	97.0
7	4	1.35 ($n = 5$)	0.34	95.8	97.6

[a] Trypan blue assay. [b] Reported for 0% (v/v).

Table 4 Cell viability of P388 cells incubated for prolonged times with 7% (v/v) Mn–M48SNs

% Mn–M48SNs (v/v)	Incubation time (h)	Mean number of cells $\times 10^5$	Standard dev. $\times 10^5$	Mean viability[a] (%)	Relative mean viability[b] (%)
7	0	8.25 ($n = 8$)	0.98	98.2	100
7	12	8.68 ($n = 4$)	1.47	99.0	100
7	24	9.21 ($n = 4$)	0.68	96.6	98.4

[a] Trypan blue assay. [b] Reported for 7% (v/v) Mn–M48SNs at 0 h.

In Mn–M48SNs suspended in water and in borate buffer, there was no evidence of a second inflexion in the low magnetic field strength range (<0.5 MHz), typical of the isotropic "contact" interaction between the electron spin of Mn^{2+} and protons in the first hydration shell.[80,81] This low magnetic field inflexion, observed for free Mn^{2+} ions, is due to the delocalization of the electronic wave function of hydrated Mn^{2+} ions, to such an extent that a significant amount of its spin extends to the water protons of the first hydration shell.[82] Only Mn–M48SN nanoparticles incubated in an acetate buffer clearly showed the low-magnetic field strength inflexion (Fig. S8†), revealing thereby some leaching of Mn^{2+} ions from the M48SN structures. Higher T_1/T_2 (~4 at 40 MHz) ratios were also noted in acetate-incubated Mn–M48SNs (T_2 data not shown), which also points to the fact that the contact interaction of Mn^{2+} ions affects the transversal relaxivity of the suspensions, as expected for Mn^{2+}-containing suspensions. Very high r_2/r_1 ratios (~10) are indeed measured for aqueous solutions containing free Mn^{2+} ions, which is clearly not the case for Mn–MSN suspensions incubated in water and in borate buffers.[49,73] Hence, the use of an acetate buffer as an incubation medium to reproduce the endosomal conditions (in particular the pH) appears questionable since its reactivity with the manganese oxide, hydroxide or silicate structures leads to Mn^{2+} leaching. Thus, the results of this study point to the necessity of using aqueous media with properties as close as possible to those in the cell vesicles, and therefore not necessarily based on acetate. The slight upward turn in the high-field region (20–30 MHz), typical of paramagnetic nanoparticles, such as ultra-small MnO, was also observed with Mn–M48SNs in water and borate buffers.[49] This signature indicates that electronic relaxation time, increasing with the magnetic field strength, could be an important limiting factor in that range. Finally, the decrease of relaxivity above 30 MHz is attributed to dipolar dispersion.

3.5. Cell labelling and MRI studies

Drug delivery to brain tumours is a medical challenge for which mesoporous silica particles could provide promising solutions. For example, it is well known that brain tumours represent a chemoattractive environment, which is colonized by microglia and by monocyte-derived macrophages.[83] As a result, macrophages may represent a potential vector to bring anti-tumoral therapy into the tumour. The cell line P388 (phagocytic leukaemia line) has been extensively used in experiments aiming at visualising the delivery of monocytes/macrophages to brain tumour areas, following intravenous injections of these cells.[84] Therefore, P388 cells represent an interesting cell line in the perspective of evaluating the potential of Mn–M48SNs for *in vivo* cell tracking and for macrophage-mediated drug delivery applications.

The tolerance of P388 cells to Mn–M48SNs was assessed using escalating concentrations of nanoparticles (0, 0.12, 0.29, 0.41, corresponding to 0, 2, 5, and 7% (v/v), respectively) and an incubation time of 4 hours. At all concentrations, the viability of

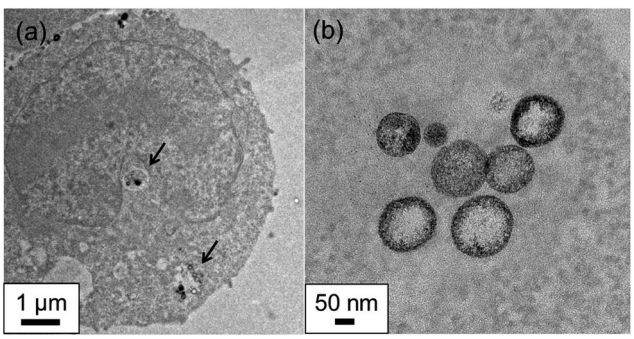

Fig. 7 TEM images (200 keV) of (a) P388 cells labelled with Mn–M48SNs; (b) nanoparticles taken up in vesicles, showing indications of a Mn radial concentration profile in the porous particles.

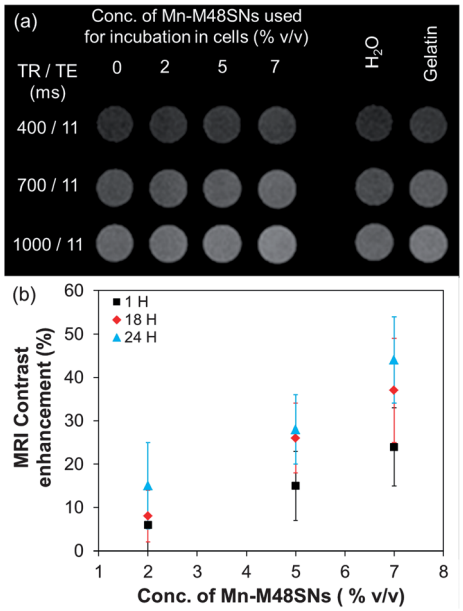

Fig. 8 P388 cells labelled with Mn–M48SNs: (a) T_1-w. MR images of cells incubated for 4 h with 0, 2, 5 and 7% (v/v) stock solutions of Mn–M48SNs obtained with different echo delay times and repetition times; (b) contrast-enhancement in P388 labelled cells suspended in gelatine was monitored by MRI for up to 24 h.

cells was 95% and higher (Table 3). A series of cell samples incubated for 4 hours with high concentrations of particles (7% (v/v)) were incubated further in a fresh complete medium for up to 24 h (after the end of incubation with Mn–M48SNs). Results from this experiment are displayed in Fig. S9 (ESI).† Compared with control cells, incubation with Mn–M48SNs delayed the proliferation in the first hours after the end of incubation. However, after 24 hours, the difference in cell number between both cell culture groups was not statistically different. At every time point, cell viability was systematically measured: for incubated cells, the viability was always higher than 97.1%. Finally, in order to measure the impact of prolonged incubation with high concentrations of Mn–M48SNs, cells were incubated for 12 h and 24 h, harvested, counted and their viability was measured (Table 4). No significant difference in cell numbers was noted, and the viability of cells was higher than 96.6% at all time points (0, 12 h and 24 h). Therefore, we concluded that incubation with high concentrations of Mn–M48SNs (7% (v/v)) neither affects cell proliferation nor cell viability.

The presence of nanoparticles inside cells was confirmed by TEM investigations. A shown in Fig. 7, the mesoporous silica particles were clearly visible in the cells, mainly as small clusters of nanoparticles (<10 particles). The particles appeared more contrasted than the rest of the cells, both due to the silica, and more importantly to the presence of electron-dense manganese. Overall, the apparent concentration of nanoparticles internalised in cells was not very high, and points to the necessity of providing a surface treatment to the nanoparticles to enhance cell uptake in the perspective of establishing efficient cell labelling procedures. In the present study, only passive nanoparticle internalisation was studied. TEM visualisation also confirmed the separation of labelled cells from non-internalised nanoparticles present in the cell culture medium. Indeed, there was no evidence of nanoparticles outside the cells, or attached at the surface of the cells. This assessment was important to validate that MRI contrast enhancement results were not contaminated with non-internalised nanoparticles.

Mn–M48SN-labelled cells were then suspended in gelatine, distributed in cell culture wells, and visualised by T_1-weighted MRI (Fig. 8a) at minimum echo time (TE) and at three different repetition times (TR). The concentration of cells per μL of 0, 2, 5 and 7% (v/v) correspond to 1.07×10^4 cells per μL, 1.13×10^4 cells per μL, 0.89×10^4 cells per μL and 0.68×10^4 cells per μL respectively. The highest concentration of CA (7% (v/v)) provides the most significant MRI contrast effect despite the lowest concentration of cells suggesting a higher internalisation rate. The cells were kept under incubation for up to 24 h, and imaged at different time points. In spite of the rather low uptake of Mn–M48SNs in cells, the contrast between labelled cells and unlabelled cells was clearly visible. For 7% and 5% (v/v) incubation samples, 10–50% contrast enhancements were noted. A control experiment was performed with 7% (v/v) M48SNs (without Mn) that did not reveal any contrast enhancement (Fig. S10, ESI†). The quantified contrast (Fig. 8b) revealed that all samples labelled with 5% and 7% (v/v) Mn–M48SN suspensions, as well as those labelled with 2% (v/v) after 24 h, showed significantly higher "positive" contrast compared to unlabelled cell samples. In fact, a general trend toward slightly higher contrast enhancement was noted over time (up to 24 h), most probably reflecting the modifications of the nanoparticles, as evidenced *in vitro*, *e.g.*, hydroxylation of Mn-lined nanopores. A massive leakage of Mn^{2+} ions from the nanoparticles would have resulted in lower r_1, and much higher r_2/r_1 ratios, and therefore to a pronounced decrease of the "positive" contrast enhancement in T_1-w. MRI.

4. Conclusions

Mesoporous silica nanoparticles of narrow size distribution and exhibiting a 3-D pore network were synthesized, and impregnated with Mn in the perspective of being used as "positive" MRI contrast agents for cell labelling studies. Open porosity and optimal distribution of Mn in M48SNs allowed high relaxivities ($r_1 = 8.4\ mM^{-1}\ s^{-1}$) and low r_2/r_1 ratios *in vitro*, as well as an efficient contrast enhancement in cells (*in vivo*). After suspension in water, evidence was found that Mn did not leach as free Mn^{2+}, even under acidic conditions, but rather rearranged into Mn–OOH structures with Mn(II) as the main oxidation state. Mn–M48SN suspensions have a relaxivity at least 4–5 times higher than those of common Mn chelates, with very low r_2/r_1 ratios (~2), which is exceptional for a Mn-based MR contrast agent. These relaxometric properties provide remarkably good "positive" contrast enhancement properties to the MSN-labelled nanostructures that can thus be used to label cells without significantly affecting their viability. A clear positive contrast was evidenced in MRI with labelled cells, even for low numbers of particles internalized per cell. Because Mn^{2+} ions are increasingly used in neurological studies (MEMRI), Mn–M48SN particles could therefore be employed as an interesting system

to label neurological and immune cells, and to progressively deliver Mn^{2+} ions at low doses and under controlled biological environments. The porosity could also be used to deliver complementary biological factors or drugs. Future studies will aim at investigating the thresholds of Mn^{2+} leaching necessary to maximize MRI contrast enhancement, while minimizing the impact on cell viability.

Acknowledgements

This study was supported by the Centre Québécois des Matériaux Fonctionnels (CQMF), the Fonds de la recherche sur la nature et les technologies du Québec (FQRNT), and NSERC Discovery grants (M.A.F. and F.K.). Dr Luce vander Elst (U. Mons), Dr Robert Muller (U. Mons), Marie-France Côté, Jacques Lacroix and Andrée-Anne Guay-Bégin (CHUQ) and Vicky Dodier (U. Laval) are gratefully acknowledged for their valuable contribution to this work.

Notes and references

1 W. J. Rogers, C. H. Meyer and C. M. Kramer, *Nat. Clin. Pract. Cardiovasc. Med.*, 2006, **3**, 554.
2 L. Josephson, C.-H. Tung, A. Moore and R. Weissleder, *Bioconjugate Chem.*, 1999, **10**, 186.
3 C. Corot, P. Robert, J.-M. Idée and M. Port, *Adv. Drug Delivery Rev.*, 2006, **5**, 1471.
4 C. Heyn, J. A. Ronald, L. T. Mackenzie, I. C. MacDonald, S. F. Chambers, B. K. Rutt and P. J. Foster, *Magn. Reson. Med.*, 2006, **55**, 23.
5 S. Metz, G. Bonaterra, M. Rudelius, M. Settles, E. J. Rummeny and H. E. Daldrup-Link, *Eur. Radiol.*, 2004, **14**, 1851.
6 R. N. Muller, L. Vander Elst, A. Roch, J. A. Peters, E. Csajbok, P. Gillis and Y. Gossuin, *Adv. Inorg. Chem.*, 2005, **57**, 239.
7 H. E. Daldrup-Link, M. Rudelius, R. A. Oostendorp, V. R. Jacobs, G. H. Simon, C. Gooding and E. J. Rummeny, *Acad. Radiol.*, 2005, **12**, 502.
8 J. W. M. Bulte and D. L. Kraitchman, *NMR Biomed.*, 2004, **17**, 484.
9 M. Bottrill, L. Kwok and N. J. Long, *Chem. Soc. Rev.*, 2006, **35**, 557.
10 H. B. Na, I. C. Song and T. Hyeon, *Adv. Mater.*, 2009, **21**, 2133.
11 H. B. Na and T. Hyeon, *J. Mater. Chem.*, 2009, **19**, 6267.
12 P. Caravan, J. J. Ellison, T. J. McMurry and R. B. Lauffer, *Chem. Rev.*, 1999, **99**, 2293.
13 E. Toth, L. Helm and A. E. Merbach, *Top. Curr. Chem.*, 2002, **221**, 61.
14 G. De Stasio, P. Casalbore, R. Pallini, B. Gilbert, F. Sanita, M. T. Ciotti, G. Rosi, A. Festinesi, L. M. Larocca, A. Rinelli, D. Perret, D. W. Mogk, P. Perfetti, M. P. Mehta and D. Mercanti, *Cancer Res.*, 2001, **61**, 4272.
15 G. De Stasio, D. Rajesh, P. Casalbore, M. Daniels, R. Erhardt, B. Frazer, L. Wiese, K. Richter, B. Sonderegger, B. Gilbert, S. Schaub, R. Cannara, J. Crawford, M. Gilles, T. Tyliszczak, J. Fowler, L. Larocca, S. Howard, D. Mercanti, M. Mehta and R. Pallini, *Neurol. Res.*, 2005, **27**, 387.
16 C. Cabella, S. Geninatti Crich, D. Corpillo, A. Barge, C. Ghirelli, E. Bruno, V. Lorusso, F. Uggeri and S. Aime, *Contrast Media Mol. Imaging*, 2006, **1**, 23.
17 J.-L. Bridot, A.-C. Faure, S. Laurent, C. Rivière, C. Billotey, B. Hiba, M. Janier, V. Josserand, J.-L. Coll, L. V. Elst, R. Muller, S. Roux, P. Perriat and O. Tillement, *J. Am. Chem. Soc.*, 2007, **129**, 5076.
18 L. Faucher, M. Tremblay, J. Lagueux, Y. Gossuin and M.-A. Fortin, *ACS Appl. Mater. Interfaces*, 2012, **4**, 4506.
19 F. Evanics, P. R. Diamente, F. C. J. M. van Veggel, G. J. Stanisz and R. S. Prosser, *Chem. Mater.*, 2006, **18**, 2499.
20 Q. Ju, D. Tu, Y. Liu, R. Li, H. Zhu, J. Chen, Z. Chen, M. Huang and X. Chen, *J. Am. Chem. Soc.*, 2012, **134**, 1323.
21 H. Hifumi, S. Yamaoka, A. Tanimoto, D. Citterio and K. Suzuki, *J. Am. Chem. Soc.*, 2006, **128**, 15090.
22 W. Ren, G. Tian, L. Zhou, W. Yin, L. Yan, S. Jin, Y. Zu, S. Li, Z. Gu and Y. Zhao, *Nanoscale*, 2012, **4**, 3754.
23 Y. Liu and N. Zhang, *Biomaterials*, 2012, **33**, 5363.
24 A. E. Garcia-Bennett, *Nanomedicine*, 2011, **6**, 867.
25 Z. Li, J. C. Barnes, A. Bosoy, J. F. Stoddart and J. I. Zink, *Chem. Soc. Rev.*, 2012, **41**, 2590.
26 P. Yang, S. Gai and J. Lin, *Chem. Soc. Rev.*, 2012, **41**, 3679.
27 J. M. Rosenholm, C. Sahlgren and M. Linden, *Nanoscale*, 2010, **2**, 1870.
28 J. A. Peters and K. Djanashvili, *Eur. J. Inorg. Chem.*, 2012, **12**, 1961.
29 W. X. Mai and H. Meng, *Integr. Biol.*, 2013, **5**, 19.
30 T. Asefa and Z. Tao, *Chem. Res. Toxicol.*, 2012, **25**, 2265.
31 T. Kim, E. Momin, J. Choi, K. Yuan, H. Zaidi, J. Kim, M. Park, N. Lee, M. T. McMahon, A. Quinones-Hinojosa, J. W. Bulte, T. Hyeon and A. A. Gilad, *J. Am. Chem. Soc.*, 2011, **133**, 2955.
32 Y.-K. Peng, C.-W. Lai, C.-L. Liu, H.-C. Chen, Y.-H. Hsiao, W.-L. Liu, K.-C. Tang, Y. Chi, J.-L. Hsiao, K.-E. Lim, H.-E. Liao, J.-J. Shyue and P. T. Chou, *ACS Nano*, 2011, **5**, 4177.
33 Z. Xu, C. Li, P. Ma, Z. Hou, D. Yang, X. Kang and J. Lin, *Nanoscale*, 2011, **3**, 661.
34 X. Kang, Z. Cheng, D. Yang, P. Ma, M. Shang, C. Peng, Y. Dai and J. Lin, *Adv. Funct. Mater.*, 2012, **22**, 1470.
35 Y.-S. Lin, Y. Hung, J.-K. Su, R. Lee, C. Chang, M.-L. Lin and C.-Y. Mou, *J. Phys. Chem. B*, 2004, **108**, 15608.
36 K. M. L. Taylor, J. S. Kim, W. J. Reiter, H. An, W. Lin and W. Lin, *J. Am. Chem. Soc.*, 2008, **130**, 2154.
37 R. Guillet-Nicolas, J.-L. Bridot, Y. Seo, M.-A. Fortin and F. Kleitz, *Adv. Funct. Mater.*, 2011, **21**, 4653.
38 J. J. Davis, W.-Y. Huang and G.-L. Davies, *J. Mater. Chem.*, 2012, **22**, 22848.
39 W.-I. Lin, C.-Y. Lin, Y.-S. Lin, S.-H. Wu, Y.-R. Huang, Y. Hung, C. Chang and C.-Y. Mou, *J. Mater. Chem. B*, 2013, **1**, 639.
40 F. Carniato, L. Tei, A. Arrais, L. Marchese and M. Botta, *Chem.–Eur. J.*, 2013, **19**, 1421.
41 J.-K. Hsiao, C.-P. Tsai, T.-H. Chung, Y. Hung, M. Yao, H.-M. Liu, C.-Y. Mou, C.-S. Yang, Y.-C. Chen and D.-M. Huang, *Small*, 2008, **4**, 1445.
42 X. Huang, F. Zhang, S. Lee, M. Swierczewska, D. O. Kiesewetter, L. Lang, G. Zhang, L. Zhu, H. Gao, H. S. Choi, G. Niu and X. Chen, *Biomaterials*, 2012, **33**, 4370.

43 Y. Shen, Y. Shao, H. He, Y. Tan, X. Tian, F. Xie and L. Li, *Int. J. Nanomed.*, 2013, **8**, 119.
44 S. K. Saxena, M. Sharma, M. Patel and D. Oreopoulos, *Int. Urol. Nephrol.*, 2008, **40**, 715.
45 P. C. Lauterbur, *Nature*, 1973, **242**, 190.
46 A. P. Koretsky and A. C. Silva, *NMR Biomed.*, 2004, **17**, 527.
47 J. Crossgrove and W. Zheng, *NMR Biomed.*, 2004, **17**, 544.
48 S. Boretius and J. Frahm, *Methods Mol. Biol.*, 2011, **771**, 531.
49 M. Létourneau, M. Tremblay, L. Faucher, D. Rojas, P. Chevallier, Y. Gossuin, J. Lagueux and M.-A. Fortin, *J. Phys. Chem. B*, 2012, **116**, 13228.
50 Y. Chen, H. Chen, S. Zhang, F. Chen, S. Sun, Q. He, M. Ma, X. Wang, H. Wu, L. Zhang, L. Zhang and J. Shi, *Biomaterials*, 2012, **33**, 2388.
51 Y. Chen, Q. Yin, X. Ji, S. Zhang, H. Chen, Y. Zheng, Y. Sun, H. Qu, Z. Wang, Y. Li, X. Wang, K. Zhang, L. Zhang and J. Shi, *Biomaterials*, 2012, **33**, 7126.
52 J. M. Rosenholm, V. Mamaeva, C. Sahlgren and M. Linden, *Nanomedicine*, 2012, **7**, 111.
53 W. Zhang, J. Wang, P. T. Tanev and T. J. Pinnavaia, *Chem. Commun.*, 1996, 979.
54 M. Yonemitsu, Y. Tanaka and M. Iwamoto, *Chem. Mater.*, 1997, **9**, 2679.
55 Y.-F. Han, F. Chen, Z. Zhong, K. Ramesh, L. Chen and E. Widjaja, *J. Phys. Chem. B*, 2006, **110**, 24450.
56 S. Gomez, O. Giraldo, L. J. Garces, J. Villegas and S. L. Suib, *Chem. Mater.*, 2004, **16**, 2411.
57 X. P. Dong, W. H. Shen, Y. F. Zhu, L. M. Xiong and J. L. Shi, *Adv. Funct. Mater.*, 2005, **15**, 955.
58 T. W. Kim, P. W. Chung, I. I. Slowing, M. Tsunoda, E. S. Yeung and V. S.-Y. Lin, *Nano Lett.*, 2008, **8**, 3724.
59 P. I. Ravikovitch and A. V. Neimark, *J. Phys. Chem. B*, 2001, **105**, 6817.
60 A. V. Neimark and P. I. Ravikovitch, *Microporous Mesoporous Mater.*, 2001, **44–45**, 697.
61 I. Izquierdo-Barba, M. Colilla, M. Manzano and M. Vallet-Regi, *Microporous Mesoporous Mater.*, 2010, **132**, 442.
62 V. Cauda, C. Argyo and T. Bein, *J. Mater. Chem.*, 2010, **20**, 8693.
63 Q. Feng, H. Kanoh and K. Ooi, *J. Mater. Chem.*, 1999, **9**, 319.
64 H. Q. Sun, X. D. Qin and F. Zaera, *J. Phys. Chem. Lett.*, 2011, **2**, 2525.
65 H. W. Nesbitt and D. Banerjee, *Am. Mineral.*, 1998, **83**, 305.
66 M. Chigane and M. Ishikawa, *J. Electrochem. Soc.*, 2000, **147**, 2246.
67 H. X. Sun and F. Zaera, *J. Phys. Chem. C*, 2012, **116**, 23585.
68 Y. Liu, J. Shen, Z. Chen and Y. Liu, *Desalination*, 2011, **279**, 219.
69 M. Oku, K. Wagatsuma and T. Konishi, *J. Electron Spectrosc. Relat. Phenom.*, 1999, **98**, 277.
70 F. Parmigiani and L. Sangaletti, *J. Electron Spectrosc. Relat. Phenom.*, 1999, **98**, 287.
71 M. Oku, S. Suzuki, N. Ohtsu, T. Shishido and K. Wagatsuma, *Appl. Surf. Sci.*, 2008, **254**, 5141.
72 Y.-F. Han, F. Chen, Z. Zhong, K. Ramesh, L. Chen and E. Widjaja, *J. Phys. Chem. B*, 2006, **110**, 24450.
73 D. D. Schwert, J. A. Davies and N. Richardson, *Top. Curr. Chem.*, 2002, **221**, 165.
74 A. Asokan and M. J. Cho, *J. Pharm. Sci.*, 2002, **91**, 903.
75 D. J. Reijngoud, *Trends Biochem. Sci.*, 1978, **3**, 178.
76 A. Helenius, I. Mellman, D. Wall and A. Hubbard, *Trends Biochem. Sci.*, 1983, **8**, 245.
77 P. H. Schlesinger, *Methods Cell Biol.*, 1994, **45**, 289.
78 A. S. Arbab, L. B. Wilson, P. Ashari, E. K. Jordan, B. K. Lewis and J. A. Frank, *NMR Biomed.*, 2005, **18**, 383.
79 S. H. Koenig, C. Baglin, R. D. Brown, 3rd and C. F. Brewer, *Magn. Reson. Med.*, 1984, **1**, 496.
80 R. A. Bernheim, T. H. Brown, H. S. Gutowsky and D. E. Woessner, *J. Chem. Phys.*, 1959, **30**, 950.
81 J. King and N. Davidson, *J. Chem. Phys.*, 1958, **29**, 787.
82 S. H. Koenig and R. D. Brown, 3rd, *Magn. Reson. Med.*, 1984, **1**, 478.
83 B. Badie and J. M. Schartner, *Neurosurgery*, 2000, **46**, 957.
84 S. Valable, E. L. Barbier, M. Bernaudin, S. Roussel, C. Segebarth, E. Petit and C. Remy, *Neuroimage*, 2008, **40**, 973.